

# Highly Efficient Degradation of Persistent Pollutants with 3D Nanocone TiO<sub>2</sub>-Based Photoelectrocatalysis

Rui Song,<sup>#</sup> Haibo Chi,<sup>#</sup> Qijuling Ma, Dongfeng Li, Xiaomei Wang, Wensheng Gao, Hao Wang, Xiuli Wang, Zelong Li,<sup>\*</sup> and Can Li<sup>\*</sup>



Cite This: *J. Am. Chem. Soc.* 2021, 143, 13664–13674



Read Online

ACCESS |



Metrics & More

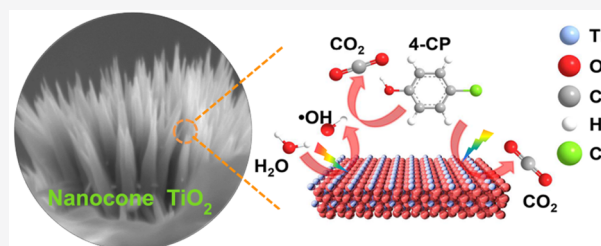


Article Recommendations



Supporting Information

**ABSTRACT:** Photoelectrocatalytic (PEC) degradation of organic pollutants into CO<sub>2</sub> and H<sub>2</sub>O is a promising strategy for addressing ever-growing environmental problems. Titanium dioxide (TiO<sub>2</sub>) has been widely studied because of its good performance and environmental benignancy; however, the PEC activity of TiO<sub>2</sub> catalyst is substantially limited due to its fast electron–hole recombination. Herein, we report a TiO<sub>2</sub> nanocone-based photoelectrocatalyst with superior degradation performance and outstanding durability. The unique conical catalyst can boost the PEC degradation of 4-chlorophenol (4-CP) with 99% degradation efficiency and higher than 55% mineralization efficiency at a concentration of 20 ppm. The normalized apparent rate constant of a nanocone catalyst is 5.05 h<sup>-1</sup> g<sup>-1</sup> m<sup>2</sup>, which is 3 times that of a nanorod catalyst and 6 times that of an aggregated particle catalyst, respectively. Further characterizations reveal that the conical morphology of TiO<sub>2</sub> can make photogenerated charges separate and transfer more efficiently, resulting in outstanding PEC activity. Moreover, computational fluid dynamics simulations indicate that a three-dimensional conical structure is beneficial for mass transfer. This work highlights that tuning the morphology of a photoelectrocatalyst at the nanometer scale not only promotes the charge transfer but also facilitates the mass transportation, which jointly enhance the PEC performance in the degradation of persistent pollutants.



## INTRODUCTION

Water pollution is threatening human beings and receiving increasing attention all around the world.<sup>1</sup> Organic pollutants from wastewater are recalcitrant and toxic, so its disposal is one of the most urgent topics in environmental research. Phenolic compounds are common persistent organic contaminants, which show non-biodegradability, posing serious risks to the environment. Some of the most toxic phenolic organics are those of chlorinated phenols, which are used as crucial intermediates in the synthesis of disinfectants, dyes, and pesticides.<sup>2,3</sup> Among them, 4-chlorophenol (4-CP) is a typical chlorinated phenol because of its widespread applications in the chlorination of organic material or the production of drugs.<sup>4,5</sup> Meanwhile, conventional biological or physical–chemical processes are ineffective in eliminating 4-CP due to its chemical stability and thermal stability.<sup>6</sup> Therefore, it is highly desirable to develop an advanced strategy for efficiently breaking down such persistent pollutants, based on the essential understanding of the degradation mechanism of pollutants.

Photoelectrocatalytic (PEC) pollutant degradation, which potentially combines the merits of both electrocatalysis and photocatalysis, is becoming one of the most promising yet challenging approaches for practical applications. Fundamentally, the separation efficiency of photogenerated charges is a

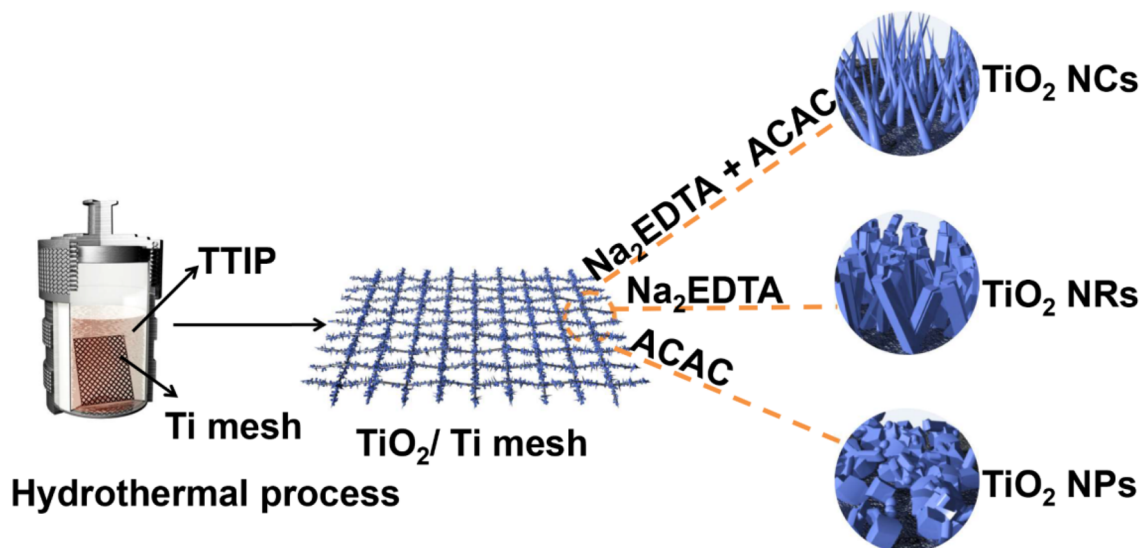
crucial factor that mainly determines the PEC performance.<sup>7</sup> Many strategies, such as heterostructure construction, nanostructure engineering, and cocatalyst modification, have been devoted to enhancing the PEC performance of the photoelectrode via improving the efficiency of charge separation in the field of photoelectrocatalysis.<sup>7</sup> Among them, building specific nanoarchitectures such as one-dimensional (1D) nanostructures (nanorods, nanotubes, nanocones, etc.) and their 3D arrays, which can dramatically reduce the recombination of electron–hole pairs through shortening the transport distance of minority charge carriers to the surface,<sup>8,9</sup> has been proved to be an effective approach to design efficient PEC systems.<sup>10</sup>

Besides the common advantages of the spatial configuration and charge separation in the 1D nanostructure, nanocone arrays possess a built-in electric field along the axial direction, which can further drive the separation of photogenerated carriers.<sup>11</sup> In addition, nanocone has more active sites

Received: May 21, 2021

Published: August 19, 2021



Scheme 1. Synthesis Scheme of TiO<sub>2</sub> Catalysts with Different Structures by a Na<sub>2</sub>EDTA-Assisted Hydrothermal Approach

compared to other 1D nanostructure with the same surface area due to more side surface of the conical structure, which will collect minority charges, thereby promoting PEC performance.<sup>12</sup> Therefore, it is important to fabricate the conical morphology of photoelectrocatalysts for efficient separation and transport of photogenerated charges.

Herein, we choose titanium dioxide (TiO<sub>2</sub>), a typical photoelectrocatalyst that has been widely investigated<sup>13,14</sup> and substantially limited by its fast electron–hole recombination,<sup>15</sup> to design a photoelectrocatalyst with a conical structure and explore how different morphologies influence the PEC performance. A TiO<sub>2</sub> photoelectrocatalyst with a 3D conical structure was prepared by a disodium ethylenediamine tetraacetate (Na<sub>2</sub>EDTA)-assisted hydrothermal approach<sup>11</sup> to eliminate persistent organic pollutants. It was found that benefiting from the significant improvement in the efficiency of charge separation and mass transport, as well as the great increase in the amount of photogenerated active species, the conical TiO<sub>2</sub> catalyst shows superior PEC performance on degradation and mineralization of 4-CP. This work offers an effective strategy to rationally design and fabricate photoelectrodes for efficient pollutant degradation.

## RESULTS AND DISCUSSION

The TiO<sub>2</sub> photoelectrocatalysts with different structure were prepared via a Na<sub>2</sub>EDTA-assisted hydrothermal approach (Scheme 1). Ti mesh was used as the substrate, which is favorable to solve the problem of poor mass transfer and surface sluggish reaction kinetics for planar devices.<sup>16,17</sup> Figure 1a shows that the TiO<sub>2</sub> synthesized with acetylacetone (ACAC) alone results in aggregated particles. In contrast, the sample fabricated in the presence of Na<sub>2</sub>EDTA displays nanorod arrays. These nanorods are well aligned and perpendicular to the substrate with diameters and lengths of 100 and 450 nm, respectively (Figure 1b). Conical structures are obtained when both ACAC and Na<sub>2</sub>EDTA are present in the hydrothermal process (Figure S1). Well-oriented TiO<sub>2</sub> nanocones with a diameter of 50 nm and a length of 1 μm are formed and distributed uniformly and densely on a Ti mesh, in a 3D structure with a highly exposed surface area (Figure 1c and d).

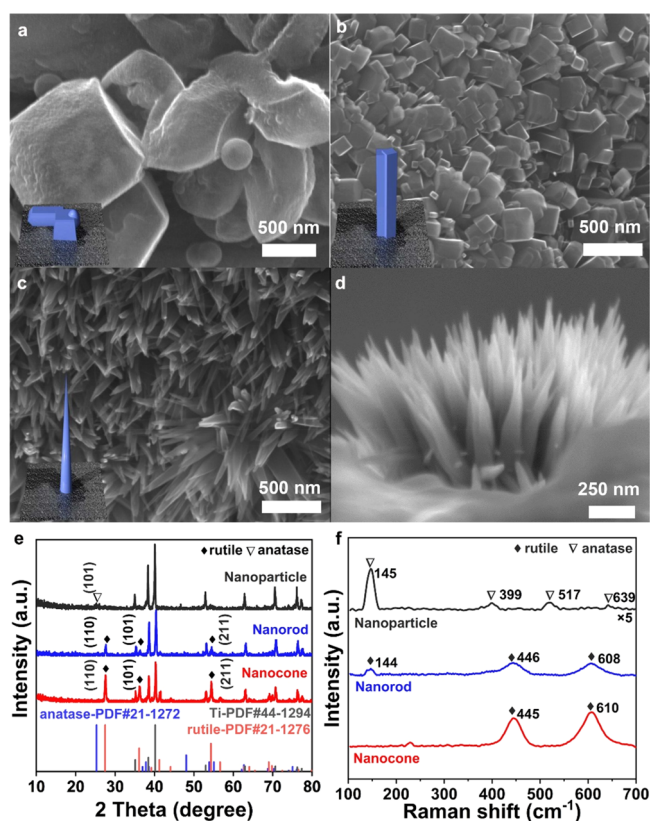


**Figure 1.** Structure characterizations of photoelectrocatalysts. SEM images of (a) aggregated particles, (b) nanorods, and (c) nanocones of TiO<sub>2</sub>. (d) SEM side views of nanocones of TiO<sub>2</sub>. (e) XRD patterns and (f) Raman spectra for TiO<sub>2</sub> photoelectrocatalysts with different structures.

Figure 1e shows the X-ray diffraction (XRD) patterns of the three different TiO<sub>2</sub> samples. The XRD peaks at 35.1°, 38.4°, and 40.1° are assigned to the (100), (002), and (101) plane of Ti mesh (JCPDS No. 44-1294). The diffraction peaks of the nanocone are indexed in accordance with the rutile structure (JCPDS No. 21-1276), and the nanorod sample exhibits typical rutile patterns as well. Apart from the diffraction peaks

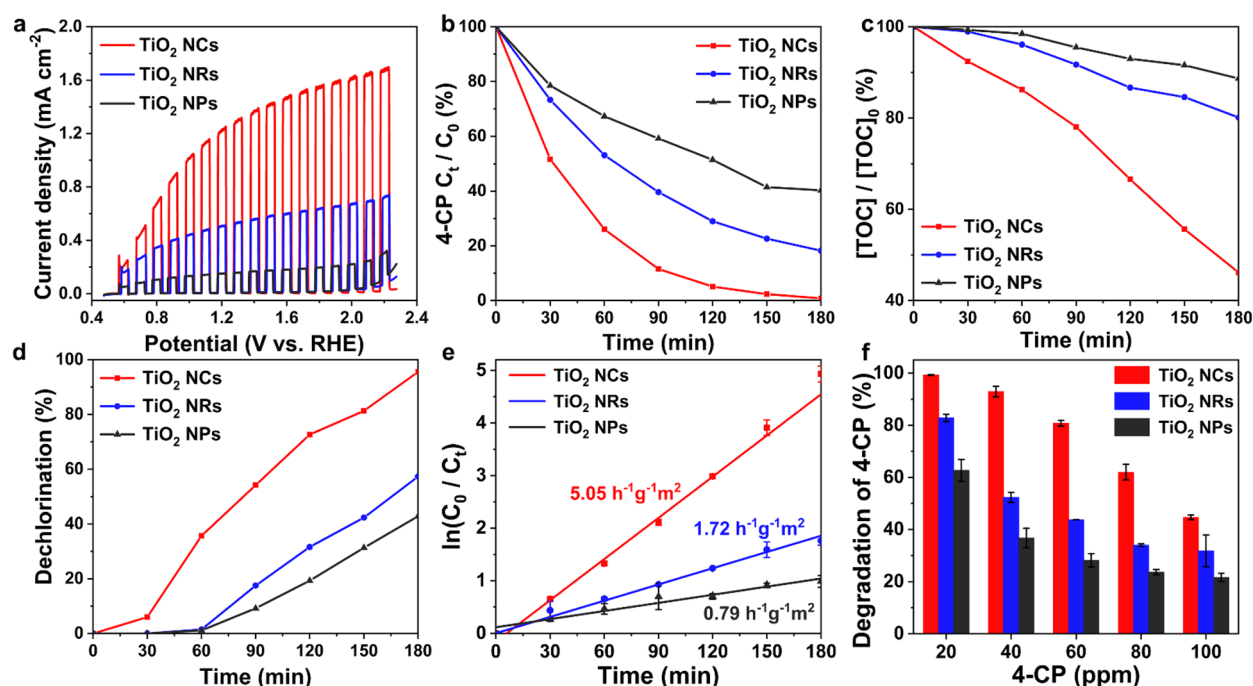


**Figure 2.** PEC performance of TiO<sub>2</sub> photocatalysts with different nanostructures. (a) Photocurrent densities of TiO<sub>2</sub> catalysts with different nanostructures, measured under chopped light. The percentage of (b) 4-CP degradation, (c) TOC removal, and (d) dechlorination for the PEC degradation process on TiO<sub>2</sub> catalysts with different nanostructures. (e) Kinetic plots of TiO<sub>2</sub> catalysts with different nanostructures for the 4-CP degradation reaction at 20 ppm. (f) Degradation of different concentrations of 4-CP on TiO<sub>2</sub> catalysts with different nanostructures.

of Ti mesh, the intensity of XRD patterns for aggregated particles is weak, and only the peak at 25.3° is visible, which corresponds to the (101) plane of anatase TiO<sub>2</sub> (JCPDS No. 21-1272). This result demonstrates that aggregated particles mainly show anatase phase with poor crystallinity.

Raman spectroscopy was then employed to further distinguish the anatase from rutile TiO<sub>2</sub>, and the results are shown in Figure 1f. The Raman bands of the nanocone at 445 cm<sup>-1</sup> (E<sub>g</sub>) and 610 cm<sup>-1</sup> (A<sub>1g</sub>) are well-resolved, confirming the rutile phase of the nanocone obtained in this work.<sup>18</sup> Moreover, the nanorod catalyst also exhibits characteristic Raman modes of rutile phase at 144 cm<sup>-1</sup> (B<sub>1g</sub>), 446 cm<sup>-1</sup> (E<sub>g</sub>), and 608 cm<sup>-1</sup> (A<sub>1g</sub>).<sup>18</sup> The enhanced Raman spectra of aggregated particles show peaks located at 145, 399, 517, and 639 cm<sup>-1</sup>, which are in accordance with characteristic anatase phase with vibrational modes of E<sub>g</sub>, B<sub>1g</sub>, A<sub>1g</sub>, and E<sub>g</sub>, respectively.<sup>19</sup> Moreover, no obvious impurity was detected in all of the TiO<sub>2</sub> catalysts (Figures S2–S4).

The PEC performance of TiO<sub>2</sub> catalysts with different structures was investigated in 0.1 M Na<sub>2</sub>SO<sub>4</sub> electrolyte with 20 ppm 4-CP under xenon lamp illumination in a conventional three-electrode cell. The photocurrents of these catalysts were recorded in the dark and under irradiation with a set of chopped linear sweeps. As shown in Figure 2a, the three TiO<sub>2</sub> catalysts show a very low dark current with respect to their photocurrents. Among the three photoelectrocatalysts, the highest anodic photocurrent was generated for the TiO<sub>2</sub> nanocone catalyst under illumination and increased steeply with increasing bias. The photocurrent of the nanocone catalyst (denoted as TiO<sub>2</sub> NCs) reaches a saturated current density of 1.68 mA cm<sup>-2</sup>, which is 2.4- and 12-fold of the photocurrent density of TiO<sub>2</sub> nanorods (denoted as TiO<sub>2</sub> NRs) and TiO<sub>2</sub> nanoparticles (denoted as TiO<sub>2</sub> NPs). The results clearly indicate the excellent PEC performance of TiO<sub>2</sub>

NCs for the degradation reaction. The transient photocurrent response to Xe lamp light of different TiO<sub>2</sub> catalysts indicates the largest amount of photogenerated carriers in TiO<sub>2</sub> NCs (Figure S6). In addition, no photocurrent decrease is observed for TiO<sub>2</sub> NCs in 3 h of illumination at 2.22 V<sub>RHE</sub> (Figure S6), whereas TiO<sub>2</sub> NRs and TiO<sub>2</sub> NPs show a dramatic decrease in performance. The decrease of photocurrent suggests that the formation and progressive accumulation of intermediates may occur on the surface of photoelectrodes.<sup>20</sup>

The PEC activities of TiO<sub>2</sub> catalysts with different structures were evaluated by monitoring the degradation of 4-CP. In order to achieve high efficiency of degradation and mineralization, the reaction potential of 2.22 V<sub>RHE</sub> was employed, even if oxygen evolution reaction (OER) occurs at such high potential (Figure S7). As shown in Figure 2b, all three catalysts are active in the degradation of 4-CP under PEC conditions. The TiO<sub>2</sub> catalysts with low surface area (0.31, 0.36, 0.39 m<sup>2</sup>/g for TiO<sub>2</sub> NCs, NRs and NPs, respectively, Table S1) show poor ability for 4-CP adsorption (Figure S10). However, the concentration of 4-CP is decreased rapidly for the TiO<sub>2</sub> NCs-based PEC degradation process, and it takes 32 min to degrade 50% 4-CP, which is much faster than TiO<sub>2</sub> NRs (67 min) and TiO<sub>2</sub> NPs (125 min). Moreover, the degradation efficiency is up to 99.3% in 180 min for TiO<sub>2</sub> NCs, which is higher than TiO<sub>2</sub> NRs (82.8%) and TiO<sub>2</sub> NPs (62.7%) in the same degradation time. The results clearly indicate that TiO<sub>2</sub> NCs show an outstanding PEC activity in the degradation reaction.

To study the degradation process of 4-CP in detail, we conducted experiments to monitor the percentage of total organic carbon (TOC) removal and dechlorination during the reaction process. We first measured the change of TOC concentration versus time during the degradation, as it can be used to describe the degree of mineralization. As shown in

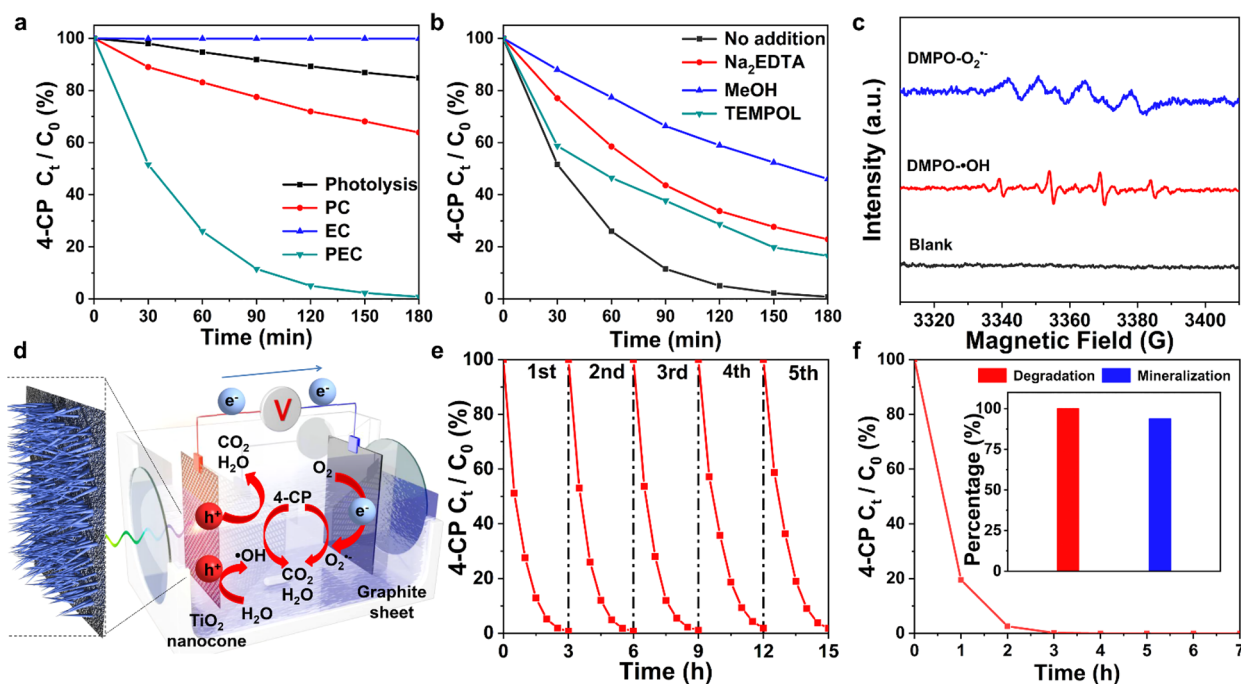


**Figure 3.** PEC performance of TiO<sub>2</sub> NCs. (a) Photoelectrocatalytic (PEC), electrocatalytic (EC), photocatalytic (PC), and direct photolysis process of 4-CP degradation on TiO<sub>2</sub> NCs. (b) Trapping experiments of active species during PEC degradation of 4-CP. (c) DMPO spin-trapping ESR spectra of •OH and O<sub>2</sub>•<sup>-</sup> in the dark and on Xe lamp light irradiation. (d) Scheme of the degradation process for the nanocone-based PEC process. (e) Cycle runs of TiO<sub>2</sub> NCs for PEC degradation of 4-CP. (f) Degradation performance of TiO<sub>2</sub> NCs with a 7 h reaction time.

Figure 2c, TiO<sub>2</sub> NCs demonstrate the efficiency of TOC removal, 54.9% in 180 min, while TiO<sub>2</sub> NRs and TiO<sub>2</sub> NPs show efficiencies of only 19.5% and 11.3%, respectively, indicating superior mineralization performance of TiO<sub>2</sub> NCs. The chlorine atom in 4-CP is turned into inorganic ions Cl<sup>-</sup> by dechlorination; thus the concentration of the Cl<sup>-</sup> generated during the 4-CP degradation process was then determined. We used the practical concentration of 4-CP as a standard example to estimate the theoretical concentration of Cl<sup>-</sup> and the percentage of dechlorination. Figure 2d shows the percentage of dechlorination in 180 min is 95.6% for TiO<sub>2</sub> NCs, which is close to complete dechlorination, while the percentages of dechlorination are 57.3% and 42.8% for TiO<sub>2</sub> NRs and TiO<sub>2</sub> NPs, respectively. The extremely low rates of dechlorination of TiO<sub>2</sub> NRs and TiO<sub>2</sub> NPs suggest that TiO<sub>2</sub> NRs and TiO<sub>2</sub> NPs catalysts are not active enough to mineralize such persistent pollutants, similar to what has been previously reported in the literature.<sup>21</sup> These results may also imply an accumulation of recalcitrant intermediates on the surface of TiO<sub>2</sub> NRs and TiO<sub>2</sub> NPs, namely, sluggish surface reaction kinetics, which usually also affects the mineralization efficiency of the catalyst.

Furthermore, the intrinsic activity of the catalysts was determined by measuring the 4-CP removal kinetics. Figure 2e shows that the data are fitted to the pseudo-first-order kinetics model. On using the specific area to normalize the apparent rate constant, the normalized constant is 5.05 h<sup>-1</sup> g<sup>-1</sup> m<sup>2</sup> for TiO<sub>2</sub> NCs, which is about 3 and 6 times that of TiO<sub>2</sub> NRs (1.71 h<sup>-1</sup> g<sup>-1</sup> m<sup>2</sup>) and TiO<sub>2</sub> NPs (0.79 h<sup>-1</sup> g<sup>-1</sup> m<sup>2</sup>), respectively. The above results clearly reveal that TiO<sub>2</sub> NCs show the highest intrinsic activity among the three catalysts in the PEC degradation of 4-CP.

We also investigated the PEC performance of catalysts when the initial concentration of 4-CP is increased in order to

understand how the mass diffusion varies with the 3D morphology of the TiO<sub>2</sub> catalysts. Figure 2f shows that as the initial concentration of 4-CP increased from 20 ppm to 100 ppm, the degradation efficiencies decreased continuously. Since the mass transfer changes with increased initial concentration of pollutant, the decrease of degradation efficiency demonstrates the crucial role of mass transfer for pollutant degradation. Meanwhile, active sites of catalysts and generated active species are exhausted by excess 4-CP; thus the degradation kinetics becomes sluggish and the amount of 4-CP removed in unit time reaches an upper limit. In this case, the TiO<sub>2</sub> NCs catalyst, which shows the best degradation efficiency at high concentrations of 4-CP, implies the highest reaction rate of the surface reaction. The above results indicate that tuning the morphology of a photoelectrocatalyst at the nanoscale can greatly influence the PEC activities through partially affecting the active sites of the catalysts, and the nanocone morphology is the most adapted to the surface reaction kinetics.

As described above, the TiO<sub>2</sub> catalyst with a nanocone morphology exhibits the highest PEC performance on the degradation reaction among the three TiO<sub>2</sub> samples with different structures. To further ascertain the superior performance of TiO<sub>2</sub> NCs, more experiments were carried out. The electrocatalytic (EC), photocatalytic (PC), and PEC process for 4-CP degradation were conducted for TiO<sub>2</sub> NCs, as shown in Figure 3a. The EC process shows an insignificant degradation efficiency of 4-CP (<1%, 180 min), and the degradation efficiency of the PC process is quite low (36.1%, 180 min), while the PEC degradation efficiency (>99%, 180 min) of TiO<sub>2</sub> NCs is much higher than the sum of EC and PC processes. This result unambiguously suggests a synergistic or cooperative effect in the TiO<sub>2</sub> NCs catalyst between the electrocatalysis and photocatalysis, and it is responsible for

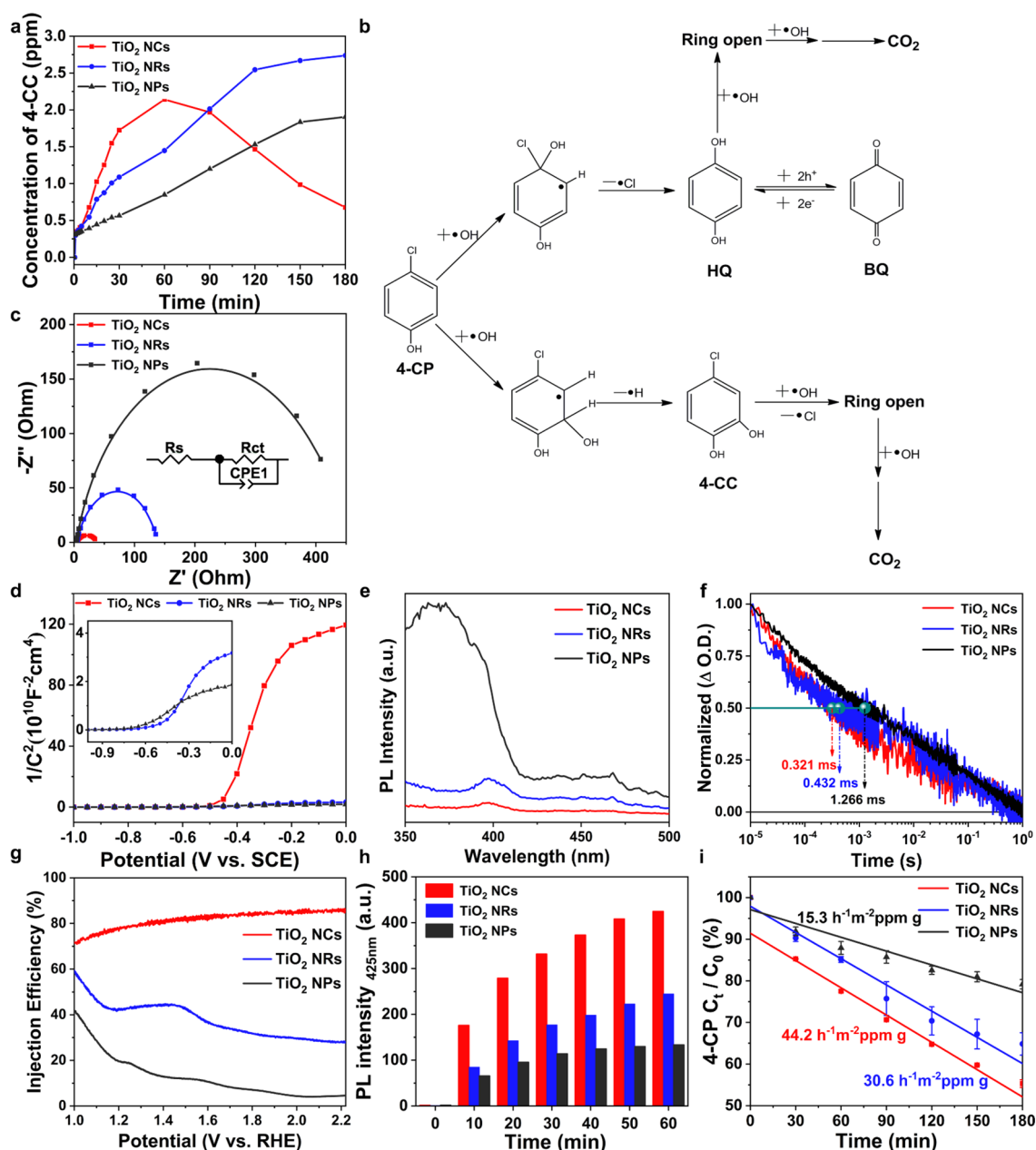


**Figure 4.** Mechanism. (a) Concentration of generated 4-CC during the degradation process. (b) Proposed degradation pathway of 4-CP during the PEC degradation on TiO<sub>2</sub> catalysts. (c) Tested (dot) and simulated (line) photo EIS spectra of different catalysts under Xe lamp illumination at 0.1 V vs SCE in a 0.1 M Na<sub>2</sub>SO<sub>4</sub> aqueous solution. The equivalent circuit is in the inset. (d) Mott–Schottky plots of TiO<sub>2</sub> catalysts with the AC potential frequency of 1000 Hz. Mott–Schottky plots for TiO<sub>2</sub> NRs and TiO<sub>2</sub> NPs are shown in the inset. (e) PL intensity of TiO<sub>2</sub> catalysts with different structures. (f) TAS spectra at 508.5 nm for TiO<sub>2</sub> photoanodes at 1.6 V<sub>RHE</sub> under illumination. (g) Injection efficiencies of TiO<sub>2</sub> catalysts with different nanostructures that are determined with and without Na<sub>2</sub>SO<sub>3</sub> (h) PL intensity of TAOH generated on TiO<sub>2</sub> catalysts with different structures. The excitation wavelength is 310 nm. (i) Kinetic plots of TiO<sub>2</sub> catalysts with different structures as the initial concentration of 4-CP is 100 ppm.

increasing the PEC performance. The synergetic effect could be explained in terms of the photogenerated charge separation (from the PC process) promoted by the applied potential (from the EC process). Similar synergetic effects are also observed in the other catalysts (Figure S12). However, their promoting effect in PEC degradation efficiency is not as obvious as for TiO<sub>2</sub> NCs. Obviously, the nanocone morphology is special in charge separation because the photogenerated charges are separated effectively when a strong built-in electric field is provided by the unique conical

structure in the nanocone catalyst, resulting in the highest PEC degradation performance.

It has been proposed that photoinduced reactive species play key roles in the oxidation of organic contaminants for organic pollutant degradation,<sup>22</sup> so the active radical species generated during 4-CP degradation were identified by quenching experiments. We used methanol (MeOH), Na<sub>2</sub>EDTA, and 4-hydroxy-2,2,6,6-tetramethylpiperidin-1-oxyl (TEMPOL) as quenchers for hydroxyl radical (<sup>•</sup>OH),<sup>23</sup> holes<sup>24</sup> and superoxide radical (O<sub>2</sub><sup>•-</sup>),<sup>25</sup> respectively. As shown in Figure 3b, when MeOH was added into the reaction system, the

efficiency of 4-CP degradation was decreased to 53.9% in 180 min, suggesting the critical role of  $\cdot\text{OH}$ . However, if  $\text{Na}_2\text{EDTA}$  was added into the solution, the degradation efficiency was reduced to 77.1%, demonstrating the presence of holes during the degradation process. Furthermore, on adding TEMPOL into the degradation system, the efficiency was suppressed slightly to 83.5%, indicating the formation of  $\text{O}_2^{\bullet-}$ . These observations reveal that the PEC degradation process on  $\text{TiO}_2$  NCs is dominated by the  $\cdot\text{OH}$  radical together with other oxidative species, holes, and  $\text{O}_2^{\bullet-}$ . Furthermore, the direct reason for the different degradation efficiencies of the three  $\text{TiO}_2$  catalysts with different structures is the different amount of reactive species on the surface of the catalysts, which will be further discussed later.

To provide direct evidence for the existence of reactive species, 5,5-dimethyl-1-pyrroline *N*-oxide (DMPO)-trapped electron paramagnetic resonance (EPR) experiments were conducted. Figure 3c displays that no characteristic EPR signals were detected in the dark, while the characteristic peaks of  $\text{DMPO}-\cdot\text{OH}$  ( $\alpha_{\text{H}} = \alpha_{\text{N}} = 14.9$  G) were observed under Xe lamp illumination.<sup>23</sup> Furthermore,  $\text{O}_2^{\bullet-}$  was captured and verified by characteristic peaks ( $\alpha_{\text{N}} = 14.3$  G,  $\alpha\beta_{\text{H}} = 11.2$  G,  $\alpha\gamma_{\text{HI}} = 1.3$  G) in MeOH solution under PEC conditions.<sup>26</sup> The formation of  $\text{O}_2^{\bullet-}$  radical can also be confirmed by the EPR signals of TEMPOL (Figure S14). The weakened intensity of characteristic peaks of TEMPOL in the EPR spectra implies that the concentration of TEMPOL is decreased after reacting with  $\text{O}_2^{\bullet-}$ .<sup>27</sup> These EPR results clearly indicate the generation of  $\cdot\text{OH}$  and  $\text{O}_2^{\bullet-}$  on  $\text{TiO}_2$  NCs during the degradation reaction.

Figure 3d illustrates the degradation process on  $\text{TiO}_2$  NCs. The nanocone  $\text{TiO}_2$  catalyst is activated by light irradiation to generate photoinduced hole and electron pairs. The generated charges are separated by the applied bias. The holes on the anode catalyst directly oxidize water and surface hydroxyl groups to produce  $\cdot\text{OH}$ ,<sup>28</sup> which then reacts with pollutants. Meanwhile, the electrons in the cathode can reduce the dissolved oxygen molecules in the solution to generate  $\text{O}_2^{\bullet-}$  radicals,<sup>24</sup> which are confirmed to be also involved in the degradation process. These active species can effectively degrade and mineralize the persistent pollutants. In short, the photogenerated holes and electrons are separated effectively in space and improve the PEC degradation performance of  $\text{TiO}_2$  NCs. The highly efficient charge separation on the nanocone catalyst should be the reason that  $\text{TiO}_2$  NCs outperform the other different morphologies of  $\text{TiO}_2$  catalysts in PEC performance.

We also investigated the stability of  $\text{TiO}_2$  NCs. Figure 3e shows that no noticeable variation on the degradation efficiency of 4-CP is observed in five cycling tests under PEC conditions. Further XRD patterns and SEM images (Figure S15) of post- $\text{TiO}_2$  NCs after 5 cycles show no distinct alteration in conical structure. These results demonstrate robust durability and resistant to light corrosion of the  $\text{TiO}_2$  NCs electrode, suggesting its potential for practical applications. Moreover, after prolonging the reaction period in 20 ppm 4-CP,  $\text{TiO}_2$  NCs exhibit a mineralization efficiency of 93.8% in 7 h (Figure 3f). On further delaying the reaction period to 12 h, the degree of mineralization can reach over 99% (Figure S14). These results suggest  $\text{TiO}_2$  NCs can degrade persistent pollutants completely.

To study the mechanism of the 4-CP degradation reaction and the difference in PEC performance for different

morphologies of  $\text{TiO}_2$  catalysts, we conducted more experiments. According to the UHPLC-MS and HPLC results (Figures S17 and S18), three different intermediates, 4-chlorocatechol (4-CC), hydroquinone (HQ), and benzoquinone (BQ), are detected and determined. The results show that all three key intermediates are generated as soon as light illumination occurs, and the quantities of each intermediate are quite different on the three  $\text{TiO}_2$  catalysts. For HQ and BQ (Figure S19), no accumulation is observed on  $\text{TiO}_2$  NCs, and both of them are destructed ultimately. However, those species are accumulated on  $\text{TiO}_2$  NRs and  $\text{TiO}_2$  NPs, and the concentration of such intermediates is higher than those of  $\text{TiO}_2$  NCs. Besides, another detected important intermediate is 4-CC, and its concentration is much higher than those of BQ and HQ. Figure 4a shows that the concentration of 4-CC increases to 2 ppm first and then decreases to 0.6 ppm on  $\text{TiO}_2$  NCs, whereas it increases continuously to 2.7 and 1.9 ppm on  $\text{TiO}_2$  NRs and  $\text{TiO}_2$  NPs.  $\text{TiO}_2$  NCs show adequate PEC degradation activities to those recalcitrant intermediates, which can be attributed to the built-in electric field provided by the unique conical morphology, resulting in efficient charge separation. Accordingly, inefficient charge separation results in poor PEC performance of the other two  $\text{TiO}_2$  photocatalysts. In addition, the total concentration of detected chlorine species (4-CC,  $\text{Cl}^-$ , and remaining 4-CP) after the degradation reaction is consistent with that of the initial 4-CP for  $\text{TiO}_2$  NCs but not in accordance for  $\text{TiO}_2$  NRs and NPs. These results indicate that there is no other chloride intermediates on  $\text{TiO}_2$  NCs, whereas still some chlorine intermediates are not detected on  $\text{TiO}_2$  NRs and  $\text{TiO}_2$  NPs. Thus, we propose the degradation pathway of 4-CP (Figure 4b) according to the reported literature<sup>6,29</sup> and the above results. Two main reaction approaches are present during the degradation process of 4-CP. Hydroxyl radicals can attack the para-position of the hydroxyl group of 4-CP and HQ is formed with a following dechlorination.<sup>30,31</sup> BQ is produced via fast electron shuttle mechanism existence between HQ and BQ.<sup>31</sup> The other approach is that hydroxyl radicals attack the ortho-position of the hydroxyl group of 4-CP to form 4-CC.<sup>32</sup> The generated intermediates can be mineralized to  $\text{CO}_2$  and  $\text{H}_2\text{O}$  by deep oxidation. Nevertheless, there are still some unknown intermediates that are not detected.

$\text{TiO}_2$  NCs show superior degradation performance not only for the initial pollutant but also for the generated intermediates. Thus, it is necessary and worthwhile to investigate the difference of catalytic activity of different morphologies of catalysts. An electrochemical impedance spectroscopy (EIS) test was carried out to study the charge transfer and recombination process at semiconductor–electrolyte interfaces.<sup>33</sup> Figure 4c shows a typical Nyquist plot obtained from the illuminated different catalysts. Compared to the dark conditions (Figure S20), the diameters of the semicircle loop on the Nyquist plot of different catalysts were decreased prominently, indicating a large number of charges generated under illumination.  $\text{TiO}_2$  NCs show a 35.9  $\Omega$  charge transfer impedance under illumination, which is much smaller than that of  $\text{TiO}_2$  NRs (137  $\Omega$ ) and  $\text{TiO}_2$  NPs (442.3  $\Omega$ ), suggesting more efficient separation of photo-generated electron–hole pairs and faster charge transfer kinetics at the interface between electrolyte and catalyst.<sup>9</sup>

We also conducted electrochemical measurements on  $\text{TiO}_2$  catalysts to determine the nature of the space charge region. Figure 4d shows that all three  $\text{TiO}_2$  catalysts with different

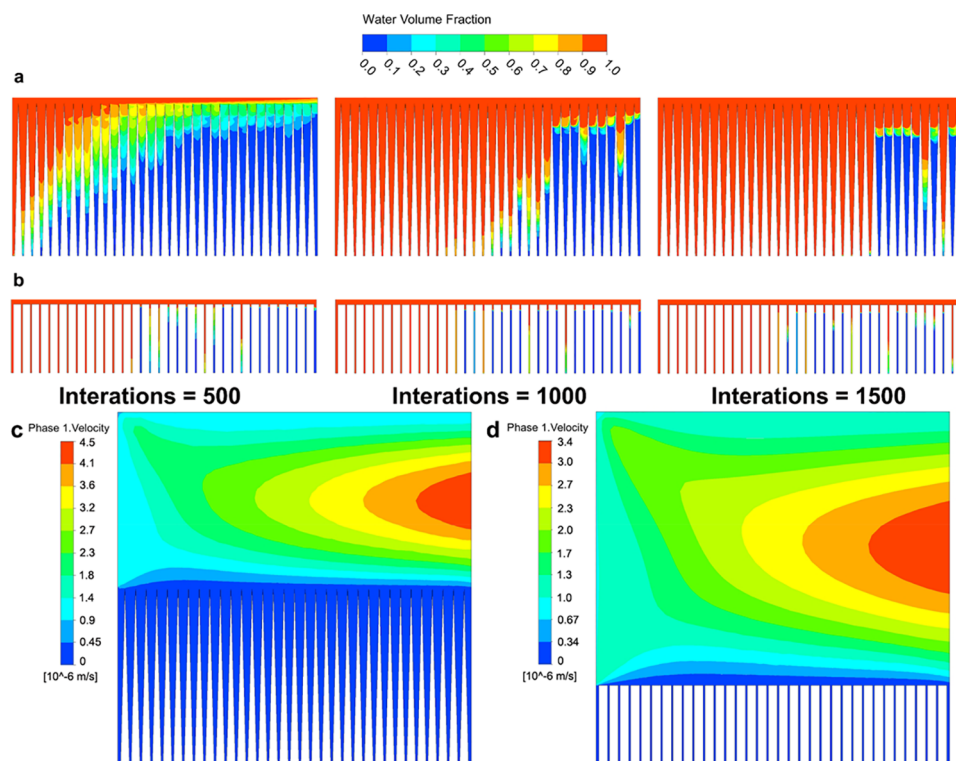


**Figure 5.** CFD simulations. The volume fraction magnitude field of water flow on (a) TiO<sub>2</sub> NCs and (b) TiO<sub>2</sub> NRs after different times of simulation. The velocity magnitude contours of water flow on (c) TiO<sub>2</sub> NCs and (d) TiO<sub>2</sub> NRs.

structures display positive slopes in Mott–Schottky plots, which indicates that the obtained TiO<sub>2</sub> catalysts are n-type semiconductors. Based on the Mott–Schottky relation (eqs 1 and 2), we can calculate the thickness of the depletion layer to describe the space charge region:<sup>34</sup>

$$N_D = (2/\epsilon_0\epsilon\epsilon_0)[d(1/C^2)/dV]^{-1} \quad (1)$$

$$W = [2\epsilon\epsilon_0(E - E_{FB})/\epsilon_0N_D]^{1/2} \quad (2)$$

where  $e_0$  is the electron charge,  $\epsilon$  is the dielectric constant of TiO<sub>2</sub> ( $\epsilon_{\text{rutile}} = 170$ ,<sup>35</sup>  $\epsilon_{\text{anatase}} = 48$ <sup>36</sup>),  $\epsilon_0$  is the permittivity of a vacuum,  $N_D$  is the donor density,  $E$  is the electrode potential, and  $E_{FB}$  is the flat band potential. When TiO<sub>2</sub> NCs contact the electrolyte, the calculated thickness is 343.23 nm (Table S1), which is much larger than that of TiO<sub>2</sub> NRs (47.66 nm) and TiO<sub>2</sub> NPs (8.86 nm), indicating the formation of the strongest built-in electric field in TiO<sub>2</sub> NCs.<sup>37</sup> In a typical n-type surface depletion layer of a photocatalyst, photogenerated minority carriers (holes) are driven to the surface and majority carriers (electrons) cannot migrate to the surface reaction centers. Therefore, electrons are scarce in the depletion region and the recombination of holes is greatly reduced.<sup>38</sup> In the case of the wide space charge region, the recombination of photogenerated charges can be reduced dramatically and the surface oxidation reaction could be greatly promoted thereby.

To reveal the dynamics on migration and separation of photogenerated electrons and holes in TiO<sub>2</sub> catalysts, photoluminescence (PL) emission spectroscopy was employed. Figure 4e shows the PL spectra of three TiO<sub>2</sub> catalysts in the wavelength range of 350–500 nm with the excitation light at 270 nm. It clearly demonstrates that the PL peak intensity of TiO<sub>2</sub> NCs is the lower than that of the other two TiO<sub>2</sub> catalysts. Since the intensity of PL is related to the

recombination of free carriers,<sup>39</sup> the low PL intensity of TiO<sub>2</sub> NCs implies a reduced recombination of carriers, which is ascribed to efficient charge separation, beneficial for achieving high PEC activity.

Figure 4f shows the normalized in situ transient absorption spectra (TAS) at 508.5 nm to investigate photoinduced hole dynamics in the three TiO<sub>2</sub> catalysts with different structures.<sup>40</sup> We find that the decay dynamics of TiO<sub>2</sub> NCs is slightly faster than TiO<sub>2</sub> NRs and TiO<sub>2</sub> NPs. The decay half-time of photogenerated holes ( $\tau_{50\%}$ , the time when the TAS amplitude decreases to half of its initial value at  $10 \mu\text{s}$ <sup>41</sup>) is estimated to be 0.321, 0.432, and 1.266 ms for TiO<sub>2</sub> NCs, TiO<sub>2</sub> NRs, and TiO<sub>2</sub> NPs, respectively (Table S1). It clearly demonstrates that the photogenerated holes for TiO<sub>2</sub> NCs survive the shortest lifetimes under PEC conditions, which is directly related to efficient charge separation and transfer processes.<sup>42</sup> Therefore, TAS results further reveal that the efficiency of charge separation and transfer is enhanced by the built-in electric field provided from the conical structure, resulting in fast transfer and efficient utilization of holes under PEC conditions, which thereby promotes the PEC performance significantly.

We used Na<sub>2</sub>SO<sub>3</sub> as a hole scavenger to determine the efficiency of the injection of charges to the electrolyte, which is another important factor influencing the PEC performance. Figure 4g shows that at the reaction potential of 2.22 V<sub>RHE</sub>, the injection efficiency of TiO<sub>2</sub> NCs is 85%, which is 3 and 7 times that of TiO<sub>2</sub> NRs (28%) and TiO<sub>2</sub> NPs (5%). This result demonstrates that the largest proportion of holes in TiO<sub>2</sub> NCs is injected into the electrolyte, which may be derived from different morphology of catalysts.<sup>43</sup>

Terephthalic acid (TA) was used to quantitatively evaluate the concentration of generated •OH radicals in the solution,<sup>44</sup> which is related to efficient utilization of holes. TA can react

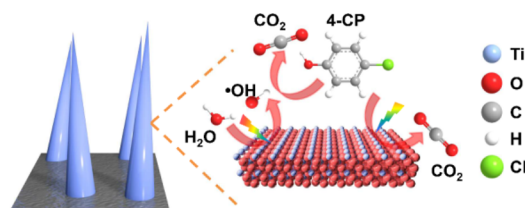
with  $\cdot\text{OH}$  to generate the fluorescent product 2-hydroxyterephthalic acid (TAOH), which can be detected by its fluorescence at 425 nm when excited with light at 310 nm.<sup>45</sup> Strong fluorescence spectra associated with TAOH are generated upon irradiation within 300–600 nm of all  $\text{TiO}_2$  catalysts (Figure S23). Figure 4h shows that the fluorescence intensity of TAOH for all catalysts increases continuously, indicating  $\cdot\text{OH}$  is generated constantly under light illumination. Meanwhile,  $\text{TiO}_2$  NCs, which are the most favorable for efficient charge separation and transfer, exhibits the highest fluorescence intensity of TAOH, demonstrating the largest amount of generated  $\cdot\text{OH}$  radicals on the surface. This result certifies that efficient charge separation and transfer are beneficial to the formation of active species, thereby enhancing the PEC degradation performance.

In order to compare the kinetics of surface reactions, we conducted experiments at a high initial concentration of 4-CP to exclude the possible influence of mass transport on the degradation kinetics. Figure 4i shows that the kinetics model is zero-order when the initial concentration of 4-CP is 100 ppm. In this case, the normalized rate constant has excluded the influence of mass transfer and the difference in surface area.  $\text{TiO}_2$  NCs exhibit a constant of  $44.2 \text{ h}^{-1} \text{ m}^{-2} \text{ ppm g}$ , which is 1.4 and 2.9 times that of  $\text{TiO}_2$  NRs ( $30.6 \text{ h}^{-1} \text{ m}^{-2} \text{ ppm g}$ ) and  $\text{TiO}_2$  NPs ( $15.3 \text{ h}^{-1} \text{ m}^{-2} \text{ ppm g}$ ), respectively, demonstrating that  $\text{TiO}_2$  NCs have the highest intrinsic activity among the three catalysts. Based on the above results, the origin of intrinsic activity can be attributed to efficient charge transport and separation, which is related to the distinct morphological structure of the catalyst.

Besides efficient charge transfer and separation, mass transport may play an important role in the degradation reaction, particularly at low concentration of the substrate molecule. Thus, we carried out computational fluid dynamics (CFD) simulations to evaluate the impact of the 3D structure on the mass transfer in the degradation process. Figure 5a and b show the volume fraction magnitude contours of water flow. It exhibits that the volume distribution of water flow in the interspace of conical structures gradually increases and the volume fraction of water in every space between neighbor cones is close to 100% finally (Figure 5a), indicating water contacts fully with the surface of  $\text{TiO}_2$  NCs. However, the volume fraction of water in nanorod arrays is lower than nanocones, and the water flow cannot fill up the interspace no matter how long the time is (Figure 5b). This result clearly demonstrates that the conical structure favors the rapid diffusion of water. Meanwhile, Figure 5c and d show the velocity magnitude contours of the fluence. The velocity of water in the interstices of nanocone arrays is  $0.45 \mu\text{m/s}$ , which is 1.3 times that of the rod structure ( $0.34 \mu\text{m/s}$ ). Faster microfluidic flow of  $\text{TiO}_2$  NCs indicates that the nanocone structure is beneficial for the mass transport for the degradation process. Since  $\text{TiO}_2$  NCs show 3 times the normalized degradation rate constant than that of  $\text{TiO}_2$  NRs, it implies again that, besides mass transfer, charge transfer and separation have a great impact on the reaction. These observations elucidate that the 3D conical structure is beneficial to enhance mass transfer.

On the basis of these results, a schematic diagram for PEC degradation of 4-CP on  $\text{TiO}_2$  NCs is proposed (Scheme 2). The nanocone structure is demonstrated to facilitate mass transfer between the interspace of the catalysts arrays. Meanwhile, benefiting from the strong built-in electric field

**Scheme 2. Schematic Diagram for PEC Degradation of 4-CP on  $\text{TiO}_2$  NCs under Illumination**



derived from distinct conical structure, the efficiency of photogenerated charge separation and transport is enhanced significantly, thus facilitating the generation of reactive species for degradation reaction. Altogether, the PEC process based on a nanocone catalyst shows outstanding performance in the degradation of persistent pollutants (Table S2).

## CONCLUSIONS

In summary, we have found that  $\text{TiO}_2$  photocatalysts with conical arrays in PEC show outstanding performance in the degradation of persistent organic pollutants, with more than 99% degradation efficiency and over 55% mineralization efficiency for 4-CP. Characterization results indicate that the superior PEC performance is attributed to efficient charge separation and mass transfer. The formation of active species for the degradation reaction is facilitated by efficient charge separation, transfer, and injection. Meanwhile, the high volume distribution fraction of water and faster water flow in space of the conical structure are beneficial to mass transfer, further facilitating the degradation process of 4-CP. Building such three-dimensional structures provides an effective strategy to achieve highly efficient PEC degradation of persistent pollutants.

## EXPERIMENTAL SECTION

**Fabrication of Photoelectrocatalysts.** Different  $\text{TiO}_2$  catalysts were synthesized by using a  $\text{Na}_2\text{EDTA}$ -assisted hydrothermal approach. Ti mesh was used as the substrate metal with dimensions of  $2.5 \times 3.5 \text{ cm}^2$  and a thickness of 0.1 cm. They were washed ultrasonically in acetone, isopropanol, ethanol, and deionized water for 30 min, respectively. Briefly, a Ti precursor containing 0.3 mL of titanium isopropoxide and 2 mL of ACAC was added into 18 mL of a 0.075 M  $\text{Na}_2\text{EDTA}$  aqueous solution. After stirring for 30 min, the solution turned transparent and was then transferred into a Teflon-lined stainless steel autoclave. The  $\text{TiO}_2$  nanocone catalyst was fabricated by hydrothermal treatment in the above solution at  $200 \text{ }^\circ\text{C}$  for 12 h. The obtained sample was washed extensively with ethanol and deionized water and then annealed in air atmosphere at  $500 \text{ }^\circ\text{C}$  for 1 h. The  $\text{TiO}_2$  catalysts with nanoparticle and nanorod structures were prepared through similar methods without  $\text{Na}_2\text{EDTA}$  and ACAC, respectively.

**Structure Characterization of Catalysts.** The crystal structure and morphology of the  $\text{TiO}_2$  catalysts were identified by XRD and scanning electron microscopy (SEM). Raman spectra of  $\text{TiO}_2$  catalysts obtained with an excitation source of 532 nm laser light were used to distinguish the anatase phase from rutile  $\text{TiO}_2$ . The surface area of  $\text{TiO}_2$  catalysts was obtained from Brunauer–Emmett–Teller surface area analysis. X-ray photoelectron spectra and energy dispersive spectroscopy were used to provide information about the surface and bulk composition of the materials. Mott–Schottky analysis was investigated at a DC potential range with an AC potential frequency of 1 kHz under dark conditions. The amplitude of the AC potential was 10 mV. EIS was conducted from 0.1 to  $10^5 \text{ Hz}$  at an alternating current signal of 10 mV. The dynamics of charge migration and separation was determined by photoluminescence (PL)

spectra and TAS. The concentration of hydroxyl radicals was investigated through the fluorescent product which was generated from TA and hydroxyl radicals. The intensity of PL of this fluorescent product was recorded by a fluorescence spectrophotometer with the excitation wavelength of 310 nm. Reactive oxygen radicals ( $\cdot\text{OH}$  and  $\text{O}_2^{\cdot-}$ ) were captured using DMPO under illumination and then was analyzed by EPR spectra.

**PEC Performance and Catalytic Analysis for Degradation Reaction.** PEC performance was evaluated in a conventional three-electrode system with a 0.1 M  $\text{Na}_2\text{SO}_4$  aqueous solution (100 mL) containing 20 ppm of 4-CP (pH = 5.67), under irradiation of a 300 W xenon lamp (Perfectlight PLS-SXE 300D, China). The system was controlled by an electrochemical workstation (Chenhua CHI760E, China), and the scan rate was 50 mV/s. The fabricated photoanode ( $7.5\text{ cm}^2$ ), a pure graphite plate ( $3 \times 5\text{ cm}^2$ ), and saturated calomel electrode (SCE) were used as the working electrode, counter electrode, and reference electrode, respectively. The measured potentials were converted to V vs RHE ( $E_{\text{RHE}} = E_{\text{SCE}} + 0.241\text{ V} + 0.059\text{ V} \times \text{pH}$ ). The distance between the working electrode and the counter electrode is 1.5 cm, and the light source is 10 cm away from the quartz cell. The practical intensity of the light source is 200 mW/ $\text{cm}^2$ .

In a typical degradation experiment, electrodes were immersed into the above solution, and the solution was stirred for 30 min to establish the adsorption–desorption equilibrium. At each time intervals, 0.7 mL of the reaction solution was withdrawn and analyzed subsequently. The potential of the degradation reaction is 2.22  $V_{\text{RHE}}$ . For the cycling tests, the catalyst was recycled after each run of the experiment by washing thoroughly with ethanol and deionized water.

The concentration of 4-CP was analyzed by high-performance liquid chromatography (HPLC, Agilent, 1260-Infinity) with a Poroshell 120 EC-C18 column and detected at a wavelength of 280 nm using a VWD detector. The mobile phase was a mixture of acetonitrile/water (30:70, v/v) at a flow rate of 1 mL/min. The concentration of intermediates was analyzed at dual detection wavelengths of 280 and 254 nm with a methanol/water mixture (50:50, v/v) as the mobile phase. Equipped with the above chromatographic column, the combination of HPLC (UltiMate 3000, ThermoFisher Scientific) and mass spectrometry (QExactive, ThermoFisher Scientific) was used to validate the intermediates. The concentration of total organic carbon was measured in a TOC analyzer (Shimadzu TOC-L). The concentration of generated chloride ion was quantified by ion chromatography (YC 7000).

**Computational Fluid Dynamics Simulation.** The flow volume fraction and velocity distribution in the electrodes were modeled by laminar equations and mixture models in CFD. For the theoretical models, the diameter of conical structures and rod arrays is consistent with the SEM results, and the distance between two neighboring nanocones or nanorods is 1.0 nm, respectively. Considering the water flow for the mesh electrode, the direction of water flow was set parallel to the substrate and perpendicular to it. To be consistent with the size of catalysts, the magnitude of the velocity was set to 1  $\mu\text{m/s}$ .

## ■ ASSOCIATED CONTENT

### SI Supporting Information

The Supporting Information is available free of charge at <https://pubs.acs.org/doi/10.1021/jacs.1c05008>.

Detailed experiments section, characterization methods, and additional PEC test methods (PDF)

## ■ AUTHOR INFORMATION

### Corresponding Authors

Zelong Li – Key Laboratory of Advanced Catalysis, Gansu Province, State Key Laboratory of Applied Organic Chemistry, College of Chemistry and Chemical Engineering,

Lanzhou University, Lanzhou, Gansu 730000, China;  
Email: [lizl@lzu.edu.cn](mailto:lizl@lzu.edu.cn)

Can Li – Key Laboratory of Advanced Catalysis, Gansu Province, State Key Laboratory of Applied Organic Chemistry, College of Chemistry and Chemical Engineering, Lanzhou University, Lanzhou, Gansu 730000, China; School of Chemical and Materials Science, University of Science and Technology of China, Hefei, Anhui 230026, China; State Key Laboratory of Catalysis, Dalian Institute of Chemical Physics, Chinese Academy of Sciences, Dalian National Laboratory for Clean Energy, The Collaborative Innovation Center of Chemistry for Energy Materials (iChEM), Dalian 116023, China; [orcid.org/0000-0002-9301-7850](https://orcid.org/0000-0002-9301-7850); Email: [canli@dicp.ac.cn](mailto:canli@dicp.ac.cn)

### Authors

Rui Song – Key Laboratory of Advanced Catalysis, Gansu Province, State Key Laboratory of Applied Organic Chemistry, College of Chemistry and Chemical Engineering, Lanzhou University, Lanzhou, Gansu 730000, China

Haibo Chi – School of Chemical and Materials Science, University of Science and Technology of China, Hefei, Anhui 230026, China; State Key Laboratory of Catalysis, Dalian Institute of Chemical Physics, Chinese Academy of Sciences, Dalian National Laboratory for Clean Energy, The Collaborative Innovation Center of Chemistry for Energy Materials (iChEM), Dalian 116023, China

Qiuling Ma – Key Laboratory of Advanced Catalysis, Gansu Province, State Key Laboratory of Applied Organic Chemistry, College of Chemistry and Chemical Engineering, Lanzhou University, Lanzhou, Gansu 730000, China

Dongfeng Li – State Key Laboratory of Catalysis, Dalian Institute of Chemical Physics, Chinese Academy of Sciences, Dalian National Laboratory for Clean Energy, The Collaborative Innovation Center of Chemistry for Energy Materials (iChEM), Dalian 116023, China; University of Chinese Academy of Sciences, Beijing 100049, China

Xiaomei Wang – Key Laboratory of Advanced Catalysis, Gansu Province, State Key Laboratory of Applied Organic Chemistry, College of Chemistry and Chemical Engineering, Lanzhou University, Lanzhou, Gansu 730000, China

Wensheng Gao – Key Laboratory of Advanced Catalysis, Gansu Province, State Key Laboratory of Applied Organic Chemistry, College of Chemistry and Chemical Engineering, Lanzhou University, Lanzhou, Gansu 730000, China;  
[orcid.org/0000-0002-8700-3831](https://orcid.org/0000-0002-8700-3831)

Hao Wang – Key Laboratory of Advanced Catalysis, Gansu Province, State Key Laboratory of Applied Organic Chemistry, College of Chemistry and Chemical Engineering, Lanzhou University, Lanzhou, Gansu 730000, China

Xiuli Wang – State Key Laboratory of Catalysis, Dalian Institute of Chemical Physics, Chinese Academy of Sciences, Dalian National Laboratory for Clean Energy, The Collaborative Innovation Center of Chemistry for Energy Materials (iChEM), Dalian 116023, China

Complete contact information is available at:

<https://pubs.acs.org/doi/10.1021/jacs.1c05008>

### Author Contributions

#R.S. and H.B.C. contributed equally.

### Notes

The authors declare no competing financial interest.

## ACKNOWLEDGMENTS

This work was supported by the Fundamental Research Funds for the Central Universities (Lzujbky-2019-60).

## REFERENCES

- (1) Bai, J.; Wang, R.; Li, Y.; Tang, Y.; Zeng, Q.; Xia, L.; Li, X.; Li, J.; Li, C.; Zhou, B. A solar light driven dual photoelectrode photocatalytic fuel cell (PFC) for simultaneous wastewater treatment and electricity generation. *J. Hazard. Mater.* **2016**, *311*, 51–62.
- (2) Du, Y.; Zhou, M.; Lei, L. Kinetic model of 4-CP degradation by Fenton/O<sub>2</sub> system. *Water Res.* **2007**, *41*, 1121–1133.
- (3) Gimeno, O.; Carbajo, M.; Beltran, F. J.; Rivas, F. J. Phenol and substituted phenols AOPs remediation. *J. Hazard. Mater.* **2005**, *119*, 99–108.
- (4) Wang, N.; Li, X.; Wang, Y.; Quan, X.; Chen, G. Evaluation of bias potential enhanced photocatalytic degradation of 4-chlorophenol with TiO<sub>2</sub> nanotube fabricated by anodic oxidation method. *Chem. Eng. J.* **2009**, *146*, 30–35.
- (5) Oudjehani, K.; Boule, P. Photoreactivity of 4-chlorophenol in aqueous solution. *J. Photochem. Photobiol., A* **1992**, *68*, 363–373.
- (6) Fu, T.; Gong, X.; Guo, J.; Yang, Z.; Liu, Y. Zn-CNTs-Cu catalytic in-situ generation of H<sub>2</sub>O<sub>2</sub> for efficient catalytic wet peroxide oxidation of high-concentration 4-chlorophenol. *J. Hazard. Mater.* **2021**, *401*, 123392.
- (7) Chen, H. M.; Chen, C. K.; Liu, R. S.; Zhang, L.; Zhang, J.; Wilkinson, D. P. Nano-architecture and material designs for water splitting photoelectrodes. *Chem. Soc. Rev.* **2012**, *41*, 5654–5671.
- (8) Hahn, N. T.; Ye, H.; Flaherty, D. W.; Bard, A. J.; Mullins, C. B. Deposition of  $\alpha$ -Fe<sub>2</sub>O<sub>3</sub> Thin Films for Photoelectrochemical Water Oxidation. *ACS Nano* **2010**, *4*, 1977–1986.
- (9) Wang, H.; Liang, Y.; Liu, L.; Hu, J.; Cui, W. Highly ordered TiO<sub>2</sub> nanotube arrays wrapped with g-C<sub>3</sub>N<sub>4</sub> nanoparticles for efficient charge separation and increased photoelectrocatalytic degradation of phenol. *J. Hazard. Mater.* **2018**, *344*, 369–380.
- (10) Wolcott, A.; Smith, W. A.; Kuykendall, T. R.; Zhao, Y.; Zhang, J. Z. Photoelectrochemical water splitting using dense and aligned TiO<sub>2</sub> nanorod arrays. *Small* **2009**, *5*, 104–111.
- (11) Zhong, D.; Cai, B.; Wang, X.; Yang, Z.; Xing, Y.; Miao, S.; Zhang, W.-H.; Li, C. Synthesis of oriented TiO<sub>2</sub> nanocones with fast charge transfer for perovskite solar cells. *Nano Energy* **2015**, *11*, 409–418.
- (12) Zhang, P.; Gao, L.; Song, X.; Sun, J. Micro- and nanostructures of photoelectrodes for solar-driven water splitting. *Adv. Mater.* **2015**, *27*, 562–568.
- (13) Hoffmann, M. R.; Martin, S. T.; Choi, W.; Bahnemann, D. W. Environmental Applications of Semiconductor Photocatalysis. *Chem. Rev.* **1995**, *95*, 69–96.
- (14) Schneider, J.; Matsuoka, M.; Takeuchi, M.; Zhang, J.; Horiuchi, Y.; Anpo, M.; Bahnemann, D. W. Understanding TiO<sub>2</sub> photocatalysis: mechanisms and materials. *Chem. Rev.* **2014**, *114*, 9919–9986.
- (15) Walter, M. G.; Warren, E. L.; McKone, J. R.; Boettcher, S. W.; Mi, Q.; Santori, E. A.; Lewis, N. S. Solar Water Splitting Cells. *Chem. Rev.* **2010**, *110*, 6446–6473.
- (16) Huang, L.; Li, D.; Liu, J.; Yang, L.; Dai, C.; Ren, N.; Feng, Y. Construction of TiO<sub>2</sub> nanotube clusters on Ti mesh for immobilizing Sb-SnO<sub>2</sub> to boost electrocatalytic phenol degradation. *J. Hazard. Mater.* **2020**, *393*, 122329.
- (17) Hankin, A.; Bedoya-Lora, F. E.; Ong, C. K.; Alexander, J. C.; Petter, F.; Kelsall, G. H. From millimetres to metres: the critical role of current density distributions in photo-electrochemical reactor design. *Energy Environ. Sci.* **2017**, *10*, 346–360.
- (18) Zhang, J.; Li, M.; Feng, Z.; Chen, J.; Li, C. UV Raman Spectroscopic Study on TiO<sub>2</sub>. I. Phase Transformation at the Surface and in the Bulk. *J. Phys. Chem. B* **2006**, *110*, 927–935.
- (19) Ohsaka, T.; Izumi, F.; Fujiki, Y. Raman spectrum of anatase, TiO<sub>2</sub>. *J. Raman Spectrosc.* **1978**, *7*, 321–324.
- (20) Liu, C.; Zhang, A. Y.; Si, Y.; Pei, D. N.; Yu, H. Q. Photochemical Anti-Fouling Approach for Electrochemical Pollutant Degradation on Facet-Tailored TiO<sub>2</sub> Single Crystals. *Environ. Sci. Technol.* **2017**, *51*, 11326–11335.
- (21) Lin, C. F.; Wu, C. H.; Onn, Z. N. Degradation of 4-chlorophenol in TiO<sub>2</sub>, WO<sub>3</sub>, SnO<sub>2</sub>, TiO<sub>2</sub>/WO<sub>3</sub> and TiO<sub>2</sub>/SnO<sub>2</sub> systems. *J. Hazard. Mater.* **2008**, *154*, 1033–1039.
- (22) Xu, J.; Zheng, X.; Feng, Z.; Lu, Z.; Zhang, Z.; Huang, W.; Li, Y.; Vuckovic, D.; Li, Y.; Dai, S.; Chen, G.; Wang, K.; Wang, H.; Chen, J. K.; Mitch, W.; Cui, Y. Organic wastewater treatment by a single-atom catalyst and electrolytically produced H<sub>2</sub>O<sub>2</sub>. *Nat. Sustain.* **2021**, *4*, 233–241.
- (23) Li, X.; Huang, X.; Xi, S.; Miao, S.; Ding, J.; Cai, W.; Liu, S.; Yang, X.; Yang, H.; Gao, J.; Wang, J.; Huang, Y.; Zhang, T.; Liu, B. Single Cobalt Atoms Anchored on Porous N-Doped Graphene with Dual Reaction Sites for Efficient Fenton-like Catalysis. *J. Am. Chem. Soc.* **2018**, *140*, 12469–12475.
- (24) Tang, H.; Shang, Q.; Tang, Y.; Yi, X.; Wei, Y.; Yin, K.; Liu, M.; Liu, C. Static and continuous flow photoelectrocatalytic treatment of antibiotic wastewater over mesh of TiO<sub>2</sub> nanotubes implanted with g-C<sub>3</sub>N<sub>4</sub> nanosheets. *J. Hazard. Mater.* **2020**, *384*, 121248.
- (25) Zheng, J.; Wang, Z.; Ma, J.; Xu, S.; Wu, Z. Development of an Electrochemical Ceramic Membrane Filtration System for Efficient Contaminant Removal from Waters. *Environ. Sci. Technol.* **2018**, *52*, 4117–4126.
- (26) Wang, L.; Lan, X.; Peng, W.; Wang, Z. Uncertainty and misinterpretation over identification, quantification and transformation of reactive species generated in catalytic oxidation processes: A review. *J. Hazard. Mater.* **2021**, *408*, 124436.
- (27) Scheinok, S.; Leveque, P.; Sonveaux, P.; Driesschaert, B.; Gallez, B. Comparison of different methods for measuring the superoxide radical by EPR spectroscopy in buffer, cell lysates and cells. *Free Radical Res.* **2018**, *52*, 1182–1196.
- (28) Wang, Y.; Hong, C.-S. Effect of hydrogen peroxide, periodate and persulfate on photocatalysis of 2-chlorobiphenyl in aqueous TiO<sub>2</sub> suspensions. *Water Res.* **1999**, *33*, 2031–2036.
- (29) Theurich, J.; Lindner, M.; Bahnemann, D. W. Photocatalytic Degradation of 4-Chlorophenol in Aerated Aqueous Titanium Dioxide Suspensions: A Kinetic and Mechanistic Study. *Langmuir* **1996**, *12*, 6368–6376.
- (30) Xu, L.; Wang, J. Magnetic nanoscaled Fe<sub>3</sub>O<sub>4</sub>/CeO<sub>2</sub> composite as an efficient Fenton-like heterogeneous catalyst for degradation of 4-chlorophenol. *Environ. Sci. Technol.* **2012**, *46*, 10145–10153.
- (31) Xu, M.; Chen, Y.; Qin, J.; Feng, Y.; Li, W.; Chen, W.; Zhu, J.; Li, H.; Bian, Z. Unveiling the Role of Defects on Oxygen Activation and Photodegradation of Organic Pollutants. *Environ. Sci. Technol.* **2018**, *52*, 13879–13886.
- (32) Lukes, P.; Locke, B. R. Degradation of Substituted Phenols in a Hybrid Gas–Liquid Electrical Discharge Reactor. *Ind. Eng. Chem. Res.* **2005**, *44*, 2921–2930.
- (33) Kang, Q.; Cao, J.; Zhang, Y.; Liu, L.; Xu, H.; Ye, J. Reduced TiO<sub>2</sub> nanotube arrays for photoelectrochemical water splitting. *J. Mater. Chem. A* **2013**, *1*, 5766–5774.
- (34) Qi, X.; She, G.; Huang, X.; Zhang, T.; Wang, H.; Mu, L.; Shi, W. High-performance n-Si/alpha-Fe<sub>2</sub>O<sub>3</sub> core/shell nanowire array photoanode towards photoelectrochemical water splitting. *Nanoscale* **2014**, *6*, 3182–3189.
- (35) Parker, R. A. Static Dielectric Constant of Rutile (TiO<sub>2</sub>), 1.6–1060 K. *Phys. Rev.* **1961**, *124*, 1719–1722.
- (36) Ohno, T.; Tokieda, K.; Higashida, S.; Matsumura, M. Synergism between rutile and anatase TiO<sub>2</sub> particles in photocatalytic oxidation of naphthalene. *Appl. Catal., A* **2003**, *244*, 383–391.
- (37) Zhang, Z.; Yates, J. T., Jr. Band bending in semiconductors: chemical and physical consequences at surfaces and interfaces. *Chem. Rev.* **2012**, *112*, 5520–5551.
- (38) Smith, W. A.; Sharp, I. D.; Strandwitz, N. C.; Bisquert, J. Interfacial band-edge energetics for solar fuels production. *Energy Environ. Sci.* **2015**, *8*, 2851–2862.

- (39) Dozzi, M. V.; D'Andrea, C.; Ohtani, B.; Valentini, G.; Selli, E. Fluorine-Doped TiO<sub>2</sub> Materials: Photocatalytic Activity vs Time-Resolved Photoluminescence. *J. Phys. Chem. C* **2013**, *117*, 25586–25595.
- (40) Kafizas, A.; Ma, Y.; Pastor, E.; Pendlebury, S. R.; Mesa, C.; Francas, L.; Le Formal, F.; Noor, N.; Ling, M.; Sotelo-Vazquez, C.; Carmalt, C. J.; Parkin, I. P.; Durrant, J. R. Water Oxidation Kinetics of Accumulated Holes on the Surface of a TiO<sub>2</sub> Photoanode: A Rate Law Analysis. *ACS Catal.* **2017**, *7*, 4896–4903.
- (41) Jing, L.; Zhou, J.; Durrant, J. R.; Tang, J.; Liu, D.; Fu, H. Dynamics of photogenerated charges in the phosphate modified TiO<sub>2</sub> and the enhanced activity for photoelectrochemical water splitting. *Energy Environ. Sci.* **2012**, *5*, 6552–6558.
- (42) Corby, S.; Francas, L.; Selim, S.; Sachs, M.; Blackman, C.; Kafizas, A.; Durrant, J. R. Water Oxidation and Electron Extraction Kinetics in Nanostructured Tungsten Trioxide Photoanodes. *J. Am. Chem. Soc.* **2018**, *140*, 16168–16177.
- (43) Dotan, H.; Sivula, K.; Grätzel, M.; Rothschild, A.; Warren, S. C. Probing the photoelectrochemical properties of hematite ( $\alpha$ -Fe<sub>2</sub>O<sub>3</sub>) electrodes using hydrogen peroxide as a hole scavenger. *Energy Environ. Sci.* **2011**, *4*, 958–964.
- (44) Nosaka, Y.; Nosaka, A. Y. Generation and Detection of Reactive Oxygen Species in Photocatalysis. *Chem. Rev.* **2017**, *117*, 11302–11336.
- (45) Wu, J. M.; Sun, Y.-G.; Chang, W.-E.; Lee, J.-T. Piezoelectricity induced water splitting and formation of hydroxyl radical from active edge sites of MoS<sub>2</sub> nanoflowers. *Nano Energy* **2018**, *46*, 372–382.